Corrosion Science 269 (2026) 113910

Contents lists available at ScienceDirect

Corrosion Science

journal homepage: www.elsevier.com/locate/corsci

Investigation of metal-solution interface during iron carbonate formation in aqueous CO_2 environment using quartz crystal microbalance

Sahithi Ayyagari [a,1], Kushal Singla [a,*,1], Kamila Turganova [a], Bruce Brown [a], Hubert Perrot [b], Srdjan Nešić [a]

[a] Institute for Corrosion and Multiphase Technology, Department of Chemical & Biomolecular Engineering, Ohio University, 342 West State Street, Athens, OH 45701, United States

[b] Sorbonne Université, CNRS, Laboratoire Interfaces et Systèmes Électrochimiques (LISE), 4, place Jussieu, UMR 8235, Paris, F-75005, France

ARTICLE INFO

Keywords:
Quartz Crystal Microbalance (QCM)
Iron carbonate ($FeCO_3$) formation
Motional resistance
Corrosion–precipitation mechanisms

ABSTRACT

The present study uses a quartz crystal microbalance (QCM) to investigate the formation of iron carbonate ($FeCO_3$) in CO_2-saturated brines. While frequency changes (Δf) measured using QCM have been traditionally used to quantify $FeCO_3$ precipitation kinetics, the associated changes in motional resistance (ΔR) are often overlooked. Here, both frequency change and motional resistance change are analyzed simultaneously to gain deeper insight into interfacial changes during the substrate corrosion and subsequent layer formation, including intermediate steps such as ion accumulation, surface dissolution, and precipitation. Experiments were conducted using quartz crystal resonators (QCR) coated with either inert gold or actively corroding iron, across varying conditions. Increase in motional resistance was observed during $FeCO_3$ layer formation on both substrates, with noticeable differences in the early-stage behavior. Transient features in ΔR appeared only in select cases and are attributed to surface-specific processes like active corrosion and local ion buildup near the QCR surface. These findings offer new perspectives on interpreting QCM data in corrosion environments and motivate the analysis of motional resistance response in future work, as it provides a useful window into the interplay between corrosion and corrosion product layer formation.

1. Introduction

Iron carbonate ($FeCO_3$) formation in carbon dioxide (CO_2) saturated aqueous environments plays an important role in the process of understanding corrosion of carbon steel infrastructure used in oil and gas production and transportation. Commonly referred to as "sweet corrosion," this process leads to the dissolution of iron from steel surfaces and the potential subsequent formation of $FeCO_3$ as a primary corrosion product in CO_2-saturated aqueous environments. $FeCO_3$ formation can be beneficial when a dense, adherent, and protective layer develops, mitigating further metal dissolution [1–6]. However, the precipitation process is influenced by a variety of environmental parameters, including saturation value $S(FeCO_3)$ temperature, pH, ionic strength, and the corrosion rate of iron [4,6–11]. Due to the complex interplay of these factors, a comprehensive understanding of $FeCO_3$ formation is essential. The overall precipitation and dissolution (reverse) reaction of $FeCO_3$ can be written as follows:

$$Fe^{2+}_{(aq)} + CO^{2-}_{3(aq)} \rightleftharpoons FeCO_{3(s)} \quad (1)$$

Precipitation of $FeCO_3$ is observed when the solution becomes supersaturated with $FeCO_3$, *i.e.*, when the solution exceeds the solubility limit of $FeCO_3$. Saturation value can be calculated using the following expression:

$$S(FeCO_3) = \frac{\left[Fe^{2+}_{(aq)}\right]\left[CO^{2-}_{3(aq)}\right]}{K_{sp}} \quad (2)$$

where K_{sp}, the solubility product of iron carbonate, is a function of temperature in Kelvin (T_K) and solution ionic strength (I_s) [11,12]:

$$K_{sp} = 10^{-\left(-59.4-0.041377T_K-\frac{2.1963}{T_K}+24.5724\log(T_K)+2.6349I_s^{0.5}-1.0027I_s\right)} \quad (3)$$

* Corresponding author.
E-mail addresses: kushal.singla.sng@gmail.com, ks661917@ohio.edu (K. Singla).
[1] shared first authorship

https://doi.org/10.1016/j.corsci.2026.113910
Received 24 January 2026; Received in revised form 31 March 2026; Accepted 5 May 2026
Available online 7 May 2026

$$I_s = \frac{1}{2}\sum_i c_i z_i^2 \quad (4)$$

where c_i is the concentration of each species in solution and z_i is the charge of the species.

$FeCO_3$ layer characterization has traditionally relied on *ex situ* methods such as weight loss measurements, scanning electron microscopy (SEM), and X-ray diffraction (XRD) [4,5,7,9,10,13–17]. While the *ex situ* techniques offer valuable insight into layer morphology and composition, they fall short in capturing the real-time dynamics of precipitation. *In situ* electrochemical techniques like linear polarization resistance (LPR) and electrochemical impedance spectroscopy (EIS) have helped bridge this gap by monitoring interfacial processes (substrate corrosion and $FeCO_3$ layer formation) in real time to understand layer formation mechanisms [4,5,7,9,10,13–23]. Recent insights from advanced *in situ* techniques have revealed transient interfacial phenomena during early-stage precipitation, offering new perspectives on nucleation behavior [7,9,13,24–27]. Yet, these do not directly detect mass accumulation on the metal surface.

Quartz crystal microbalance (QCM) offers real time monitoring of surface changes in terms of mass change by measuring resonant frequency of a quartz crystal resonator (QCR) coated with the substrate material of interest. The technique quantifies mass variation per unit area $\left(\frac{\Delta m}{A}\right)$, where mass addition leads to a decrease in frequency, while mass loss, such as from corrosion, results in an increase in frequency. This relationship is quantitatively described by the Sauerbreys' equation, applicable under the assumption of rigid surface and uniform mass change [28,29]:

$$\Delta f = -C_f \frac{\Delta m}{A} \quad (5)$$

where C_f is a constant dependent on the QCR resonance frequency (56.6 Hz·cm^2·μg^{-1} for a QCR with resonance frequency of 5 MHz). Thus, resonance frequency changes can be directly related to mass gain or loss on the crystal surface.

QCM has been successfully applied to systems ranging from copper dissolution and deposition [30,31] to zinc anode surface film formation [32], adsorption of organic corrosion inhibitors [33–37] and also passivation in biomedical alloys [38]. Among the notable contributions to the application of QCM in iron carbonate layer forming experimental systems is the work by Ma, et al., who investigated $FeCO_3$ precipitation under CO_2 corrosion conditions using gold-coated QCRs [11,12,39]. Their study primarily focused on quantifying the mass of the precipitated layer over time and correlating the data with electrochemical parameters and environmental conditions. Essentially, the frequency change due to corrosion (mass loss) and corrosion product formation (mass gain) with respect to time was used with supplementary measurements such as Fe^{2+} concentrations in the solution at various time steps during the experiment to quantify the kinetics of corrosion product formation [11,12,40]. Building on the earlier Sun & Nesic model [41], Ma, et al. [11,12] refined kinetic parameters, specifically, the activation energy and kinetic constant. These refinements improved the agreement between experimental observations and model predictions, particularly under low saturation conditions where precipitation rates are slower and more challenging to model accurately.

Beyond frequency shifts, the classical oscillatory circuit based QCM equipment used in this study can also measure motional resistance (R) with respect to time, which is a representative response related to near substrate solution properties, such as the nature and amount of added/removed mass, the interaction of added/removed mass with the near surface solution and the physical properties of the quartz crystal and the working electrode layer [42–44]. If it is assumed that the effective piezoelectric area is known and remains constant for an experiment, motional resistance change can be converted to a quantity, Gamma (Γ), which is a representation of dissipation resulting from oscillation energy losses related to the interaction of added mass within the near surface solution [43–45].

$$\Gamma = \frac{16 A e_{26}^2}{\pi} \frac{\rho_q^2 f^3}{Z_q^3} R \quad (6)$$

where A is the piezoelectrically active area (m^2), e_{26} is piezoelectric stress constant (9.65 ×10^{-2} C/m^2), ρ_q is quartz density (2650 kg/m^3), Z_q is acoustic impedance (8.8 ×10^6 kg/m^2/s), f is resonance frequency in Hz, R is motional resistance in Ohms, and Γ is in Hz.

The advantage of using Gamma change over motional resistance change is that Gamma has the same units as that of resonant frequency (Hz), which makes comparison with the measured resonance frequency change easier. For applicability of Sauerbrey's equation, mass change can be considered as a rigid mass change if $|\Delta f| >> |\Delta \Gamma|$ [43,44,46].

While Ma, et al., included measurements of motional resistance (R), this parameter received limited attention as the focus of their research was on improving the kinetic rate equation rather than elucidating mechanisms [11,12]. The relevance of R to surface interactions and energy dissipation phenomena was not fully explored, what was a missed opportunity to enhance mechanistic understanding. In context of the research presented here, subtle trends in R when analyzed in conjunction with frequency change, can reflect changes in the density and viscosity of the solution adjacent to the surface. These features are not readily detectable through change in frequency data alone.

Recognizing these complexities, the present study focuses on the interplay between mass and motional resistance responses during $FeCO_3$ formation under sweet corrosion conditions. Using QCM with both gold and iron-coated quartz crystals, the study examines how R evolves in relation to frequency shifts and environmental conditions such as substrate material, saturation level, and ionic strength. Particular attention is paid to early-time behaviors and transient interfacial phenomena that may precede $FeCO_3$ layer formation. The goal is to highlight the value in analyzing R as a critical parameter for surface processes and to encourage its routine inclusion in future QCM corrosion or similar studies.

The present study also aims to validate the application of the Sauerbrey's equation for $FeCO_3$ formation under selected conditions. This assumption, though commonly applied, had not been explicitly confirmed for these systems. In doing so, the study also emphasizes the value of motional resistance as an indicative parameter. Additionally, while most studies conducted experiments in simplified brine environments, typically involving dilute NaCl solutions [10,11,22,41], the effect of brine composition with respect to species concentrations on QCM response remains an important area for further exploration. Increasing NaCl concentration may affect both frequency and motional resistance signals and influence the properties of $FeCO_3$ layer formation [47]. Though detailed analysis will be presented in subsequent publication, preliminary results from the present study also set the stage for more complex investigations. A follow-up study will further examine the role of non-ideal electrolyte behavior, with the aim of enhancing predictive models of $FeCO_3$ layer formation under realistic field conditions.

2. Experimental procedures

2.1. Experimental setup

The QCM used in this study was the QCM200[2] model from Stanford Research Systems. QCRs with a fundamental frequency of 5 MHz were employed, purchased commercially from Inficon coated using electron beam deposition with either gold (part number: 149211–2 with coating thickness of ~0.5 μm) or pure iron (part number: 149288–1 with coating thickness of ~1 μm), unless specified otherwise. Each crystal

[2] Trade name

had an effective surface area of 1.37 cm^2. Crystals were mounted in the crystal holder, placed in a 2-liter three-electrode glass cell (Fig. 1), and served as the working electrode (WE). Volume-to-surface ratio in experiments was 14.6 mL/mm^2 which is well above the recommended value of 0.2 mL/mm^2 as per ASTM standard G31–21. A platinum coated mesh was used as the counter electrode (CE), and a saturated Ag/AgCl (KCl sat.) electrode connected via a Luggin capillary acted as the reference electrode (RE). The WE was connected to a potentiostat for electrochemical polarization when required. A pH probe, thermocouple, and CO_2 sparging tube were also inserted through the lid of the glass cell, which was designed to support all components.

The solution temperature was controlled using a thermocouple connected to a hot plate, and the cell was insulated to maintain temperature within ±1 °C. CO_2-saturated conditions were achieved by continuously sparging the solution for 4–6 h before each experiment and maintaining a continuous but reduced sparging rate throughout testing. 1 wt% or 10 wt% NaCl solutions were used as the test electrolyte. The temperature was gradually increased to 80 °C during the sparging phase. pH adjustments were made with deoxygenated 1 M HCl or 1 M NaOH prior to the start of the experiments and pH was monitored throughout the test and remained constant. Fig. 1 shows the complete assembly, including the crystal holder and glass cell configuration. The experimental setup was designed to investigate $FeCO_3$ layer formation under CO_2-saturated brine conditions using different substrates and experimental conditions to isolate the effects of corrosion and precipitation.

2.2. Methodology

Before initiating the experimental series, the QCM system was calibrated following a procedure detailed elsewhere and also repeated for this research (details in Appendix section) [11,12]. Additional quality control steps provided throughout the QCM200 operating manual were included for this study to ensure consistent and accurate performance [48]. A properly loaded crystal would give a stable frequency and motional resistance response that is specific for each material and finish of the crystal. Correctly assembled iron and gold coated quartz crystal resonators used in this research stabilized at ~5 MHz of resonance frequency and ~10 Ω of motional resistance in air. Once stable, the crystal

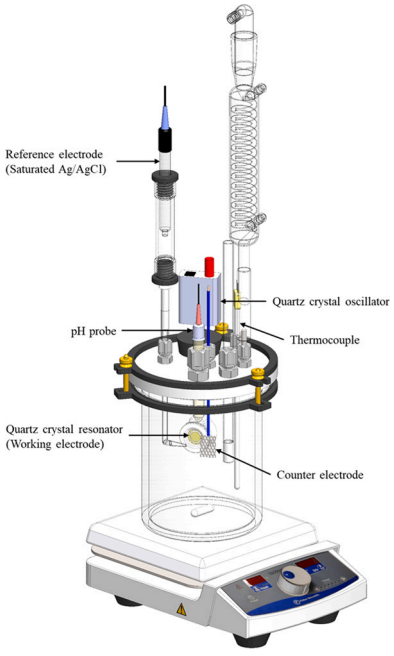

Fig. 1. Typical three electrode glass cell setup integrated with QCM with quartz crystal resonator acting as the working electrode. (Image Courtesy: Cody Shafer, ICMT).

was transferred into the test solution while still purging the experimental cell with CO_2 to minimize oxygen ingress. As a reference, introducing a QCR with resonance frequency of 5 MHz from air into deionized water at 25 °C typically causes an increase in R of approximately 300 Ω due to the much higher density and viscosity of the deionized water as compared to air.

From this baseline, experiments were conducted according to five different scenarios, designed to isolate and compare the effects of corrosion and $FeCO_3$ precipitation processes. The general idea was to use both inert (gold) and active (iron) substrates, with or without external Fe^{2+} addition, to distinguish the contributions of substrate corrosion and precipitation. Each of the five scenarios are described below with the test matrix covering all scenarios shown in Table 1.

2.2.1. Scenario (a): Bare iron corrosion at acidic pH (no precipitation)

This experiment examined corrosion alone. The solution was maintained at acidic pH 4.0 and 80 °C conditions, ensuring active substrate dissolution but preventing $FeCO_3$ formation. The iron-coated QCR was used to characterize mass loss and motional resistance changes related strictly to corrosion, providing a baseline for comparison with scenarios involving precipitation. The test was terminated when motional resistance value stopped changing.

2.2.2. Scenario (b): $FeCO_3$ formation on an iron-coated crystal driven by corrosion of substrate

This is a more complex scenario compared to Scenario (a). The selected experimental conditions (pH 6.6, 80 °C) are thermodynamically favorable for the formation of $FeCO_3$ on the substrate surface where the source of Fe^{2+} ions required for the formation of $FeCO_3$ is the corrosion of the substrate [5,6,49]. This experimental condition matches the conditions in the field where both the carbon steel corrosion and resultant $FeCO_3$ formation happen on the corroding surface simultaneously. The objective of this experiment was to analyze net mass change and motional resistance response to detect physical phenomena on/near the substrate surface when two competing processes are occurring (mass loss due to corrosion and mass gain due to corrosion product layer formation). Resonant frequency change and motional resistance were continuously monitored, and the test was terminated when a plateau in the resonance frequency change and motional resistance was approached indicating that the system had reached steady state.

2.2.3. Scenario (c): $FeCO_3$ formation on an iron coated crystal driven by bulk supersaturation

In this scenario the goal was to supersaturate the bulk solution by adding ample Fe^{2+} ions to create favorable conditions for $FeCO_3$ formation from the very beginning of the test [10–12,22,50,51]. External Fe^{2+} ions were added using a precalculated amount of deaerated $FeCl_2$ solution containing ~214 mg $FeCl_2.4H_2O$ to supersaturate the 2 liters of solution to the desired $S(FeCO_3)$ of 600 [11,51]. This scenario includes simultaneous corrosion and precipitation, but with externally controlled supersaturation level that favors rapid $FeCO_3$ formation and minimal substrate dissolution. The objective of this test was to analyze the physical responses when the mass gain on the substrate due to layer formation dominates the mass loss due to corrosion. To further achieve this, the substrate was cathodically polarized at −0.72 $V_{Ag/AgCl}$ using a potentiostat to slow down mass loss due to corrosion of the substrate. The applied potential was selected based on literature values obtained under comparable conditions. Specifically, Ayyagari et al. reported an OCP of −0.68 ± 0.01 V in 1 wt% NaCl at 80 °C [10]. This value was used as a reference, and a cathodic overpotential of −0.05 V relative to the reported OCP was applied. Under the applied cathodic polarization, the corrosion rate decreased from an initial instantaneous value of approximately 1.8 mm/year to a stabilized value of ~0.15 mm/year, confirming effective mitigation of iron dissolution. Resonant frequency

Table 1
Test matrix.

Parameter	Scenario (a)	Scenario (b)	Scenario (c)	Scenario (d)	Scenario (e)
	Bare iron corrosion	**$FeCO_3$ formation driven by corrosion**	**$FeCO_3$ formation driven by bulk supersaturation**	**$FeCO_3$ formation driven by bulk supersaturation**	**$FeCO_3$ formation driven by bulk supersaturation**
Temperature	80 °C	80 °C	80 °C	80 °C	80 °C
Electrolyte	1 wt% NaCl	1 wt% NaCl	1 wt% NaCl	1 wt% NaCl	10 wt% NaCl
pH	4.0	6.6	6.6	6.6	6.4
Working electrode	Iron-coated QCR	Iron-coated QCR	Iron-coated QCR	Gold-coated QCR	Gold-coated QCR
Polarization	-	-	- 0.72 $V_{Ag/AgCl}$	- 0.72 $V_{Ag/AgCl}$	- 0.75 $V_{Ag/AgCl}$
S($FeCO_3$)	-	-	~600 (~214 mg $FeCl_2.4H_2O$)	~600 (~214 mg $FeCl_2.4H_2O$)	~500 (~344 mg $FeCl_2.4H_2O$)
Measurements	Δf, ΔR	Δf, ΔR	Δf, ΔR	Δf, ΔR	Δf, ΔR

change and motional resistance data logging was then initiated to establish the start of the experiment.

2.2.4. *Scenario (d):* $FeCO_3$ *formation on a gold coated crystal driven by bulk supersaturation*

Use of gold substrate eliminates any mass loss step associated with corrosion of the substrate. Similar to Scenario (c), a precalculated amount of deaerated $FeCl_2$ solution was added to supersaturate the solution to the desired S($FeCO_3$) of 600 [11,51]. The gold-coated QCR was cathodically polarized at −0.72 $V_{Ag/AgCl}$ to simulate the electrochemical environment of an active steel surface without actual corrosion. The experiment included only precipitation, serving as a baseline for understanding $FeCO_3$ layer formation on inert surfaces enabling comparison with formation on actively corroding iron surfaces. Measured resonant frequency change and motional resistance were continuously monitored during the duration of test, and the test was terminated when system had reached steady state, *i.e.*, measured resonance frequency and motional resistance stopped changing with respect to time.

2.2.5. *Scenario (e):* $FeCO_3$ *formation on a gold coated crystal driven by bulk supersaturation in highly concentrated brine (10 wt%* NaCl*)*

In this scenario, 10 wt% NaCl solution at 80 °C, saturated with CO_2 was used. The initial value for the solution pH was set at 6.6. However, throughout the experiment the pH value shifted to pH 6.4. Slight deviation in the pH values (0.2 pH units) can be attributed to difficulties of precise pH measurements in highly concentrated solutions, including mismatch in ionic strengths between test solution and calibration buffers. However, in the context of this research the goal was to see the response in motional resistance which should have not been affected by the exact value of the pH as long as experimental conditions favor $FeCO_3$ formation. External Fe^{2+} ions were added using a precalculated amount of deaerated $FeCl_2$ solution containing ~344 mg $FeCl_2.4H_2O$ before the experiment for a 2-liter glass cell, and the gold substrate was cathodically polarized to −0.75 $V_{Ag/AgCl}$ to induce $FeCO_3$ precipitation. This experimental setup is analogous to Scenario (d) in terms of parameters and procedure but conducted in a higher ionic strength solution. To achieve a saturation value of 600, the concentration of CO_3^{2-} and Fe^{2+}, as well as the solubility product of $FeCO_3$ were calculated for non-ideal conditions using a concentration and ionic strength-based solution speciation model [39]. Since the activity of the bicarbonate ion changes in a non-ideal solution, an adjusted amount of $FeCl_2.4H_2O$ salt was added.

3. Results and discussion

Resonant frequency change (Δf) and motional resistance change (ΔR) are the measured values from experiments. Mass change per unit area $\left(\frac{\Delta m}{A}\right)$ and Gamma change (ΔΓ) are calculated from frequency change and motional resistance change using Eqs. (5) and (6), respectively. For applicability of Sauerbrey's Eq. (5), mass change can be considered as a rigid mass change if $|\Delta f| >> |\Delta\Gamma|$ [43,46]. Primarily for that reason, Δf and ΔΓ are plotted together as the first graph in each series as check for the use of Sauerbrey's Eq. (5).

3.1. *Scenario (a): Bare iron corrosion at acidic pH (no precipitation)*

From Fig. 2, $|\Delta f| >> |\Delta\Gamma|$, suggesting the validity of Sauerbrey's equation for conversion of measured frequency change to mass change per unit area. The analysis of the experimental data in Fig. 3 can then be used to lead us to several significant findings. A negative mass change over time is observed, indicating corrosion of the iron-coated quartz crystal resonator (QCR) under the specified conditions. The corrosion rate was calculated from the mass change of the iron layer on the crystal and amounted to about 4.4 mm/year. In comparison, the corrosion rate for carbon steel computed using the in-house corrosion prediction model (MULTICORP™) under the same conditions was ~4.0 mm/year, which is very close to the experimental value [1,52,53]. This agreement aligns with literature studies showing similar behavior in potentiodynamic polarization between pure iron and carbon steel exposed to same environmental conditions [54]. Concurrently, an increase in motional resistance is noted, possibly attributed to the formation of a Fe^{2+} ion-rich layer in the solution immediately adjacent to the resonator surface due to the corrosion of the iron substrate. This phenomenon aligns well with concepts discussed in the work by Cuenca, et al., on copper electrodeposition and electrodissolution [30,31]. The Fe^{2+} ion buildup in the boundary layer adjacent to the resonator surface is due to the influx of Fe^{2+} ions resulting from corrosion (iron dissolution), temporarily exceeding the rate of diffusion of Fe^{2+} ions away into the bulk solution. A delay is observed in the increase of motional resistance change, attributed to the time required for the buildup of the Fe^{2+} ion-rich interfacial layer. As visualized in Fig. 4, it is hypothesized that this Fe^{2+} ion-rich region manifests as a much more concentrated and viscous layer compared to the bulk solution. In the last 20 min of the

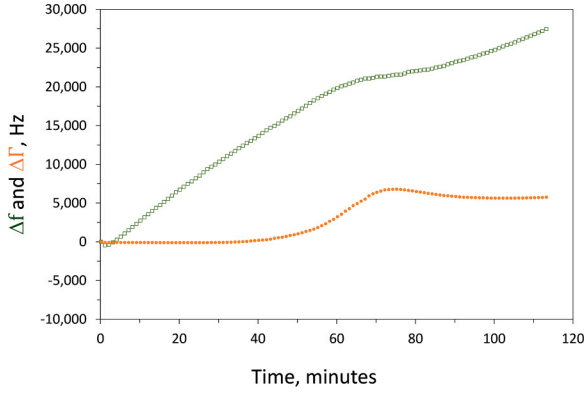

Fig. 2. Measured change in resonant frequency (open green squares) and calculated change in gamma (solid orange circles) versus time for Scenario (a) with corrosion of iron coated QCR in 1 wt% aqueous NaCl solution at 80 °C and pH 4.0.

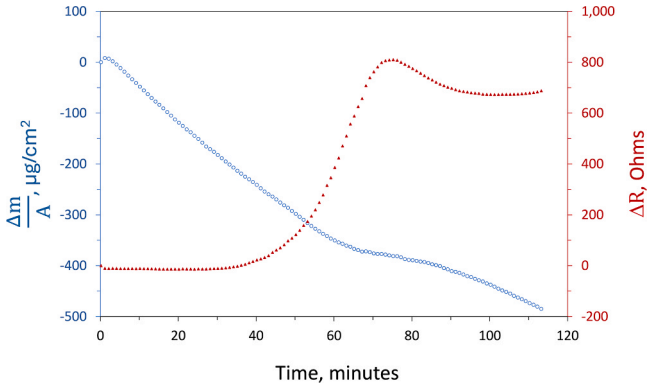

Fig. 3. Calculated change in mass per unit area (open blue circles) and measured change in motional resistance (solid red triangles) versus time for Scenario (a) with corrosion of iron coated QCR in 1 wt% aqueous NaCl solution at 80 °C and pH 4.0.

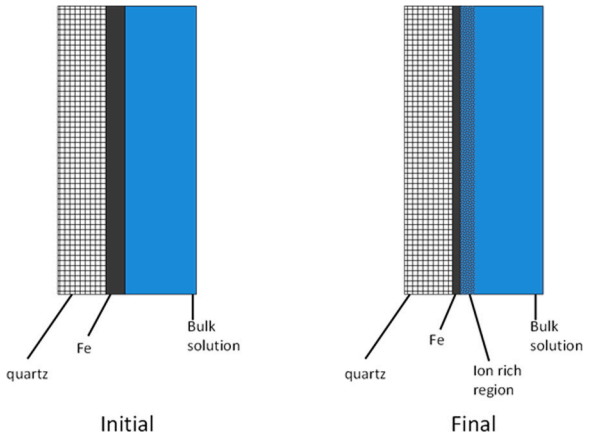

Fig. 4. Proposed schematic of the evolution of corroding QCR surface and solution near the substrate surface for Scenario (a) with freely corroding iron coated QCR.

experiment, a stabilization of the motional resistance change (ΔR) and Gamma change (ΔΓ) are observed, indicating a balance between the influx of Fe^{2+} ions into the solution immediately adjacent to the resonator surface due to corrosion and the diffusion of Fe^{2+} ions out of this region into the bulk solution. The influx of Fe^{2+} to the ion rich region is evidenced by the increase in Δf and decrease in $\frac{\Delta m}{A}$. It should be noted that corrosion of the substrate can also result in increased surface roughness, which may additionally contribute to the observed rise in motional resistance. However, it is not possible within the scope of the present study to distinguish these individual contributions. This scenario has proven that motional resistance can be used to monitor ion accumulation and interfacial changes due to change in physical properties of the solution near surface (density and viscosity), independently of the related mass change, reinforcing its value as a probe of early-stage corrosion dynamics.

3.2. *Scenario (b):* $FeCO_3$ *formation on an iron coated crystal driven by corrosion of substrate*

Fig. 5 shows the measured frequency change (Δf) and calculated Gamma change (ΔΓ) for the scenario where $FeCO_3$ corrosion product formation occurred due to corrosion of the iron substrate and environmental conditions. For experimental time less than *ca.* 25 min, the comparison of Δf to ΔΓ does not look favorable for the application of Sauerbrey's equation. However, the Sauerbrey's equation was applied in this analysis because the corroding substrate, Fe, is a rigid layer, and the frequency change measured by the quartz crystal resonator can therefore be directly related to mass changes on its surface. In this system, the observed frequency response arises from the combined effects of iron substrate corrosion and the consumption of ferrous ions during the formation of an iron carbonate layer. The initial stage of the experiment mirrors the bare iron corrosion scenario (Scenario a), where the equation has been shown to reliably capture mass loss from metal dissolution and $|\Delta f| >> |\Delta\Gamma|$. The later stage corresponds to $FeCO_3$ formation under supersaturated conditions with $S(FeCO_3) >> 1$, where the deposited or removed material behaves as a rigid, adherent layer without significant viscoelastic effects, fulfilling the assumptions of the Sauerbrey's model. This qualitative examination is aimed at shedding light on the underlying mechanistic steps and elaborating on the interfacial processes involved. In this context, the trends and characteristic features in the frequency change are more significant than the absolute numerical values presented in the plot. This is further discussed in Scenario (c). Based on the physical phenomena happening, the time axis is split into three periods in Fig. 6 which are as explained below and a schematic illustration is shown in Fig. 7.

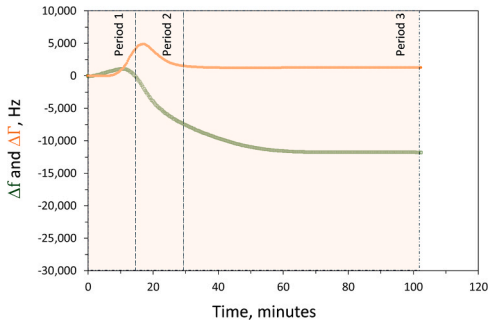

Fig. 5. Measured change in resonance frequency (open green squares) and calculated change in gamma (solid orange circles) versus time for Scenario (b) with $FeCO_3$ formation due to corrosion on iron coated QCR in 1 wt% aqueous NaCl solution at 80 °C and pH 6.6. Periods 1, 2 and 3 are described in the text.

Period 1: Mass loss is observed due to active corrosion, accompanied by a marked increase in motional resistance attributed to the formation of the Fe^{2+} rich interfacial layer near the corroding iron surface. Corrosion of QCR substrate continues until the critical conditions are reached (Fe^{2+} ion concentration is high enough at the specific environmental conditions) to cause significant precipitation of $FeCO_3$.

Period 2: There are two competing processes happening in this period. Mass loss due to corrosion of the iron substrate and mass gain due to formation of an $FeCO_3$ layer. Motional resistance decreases

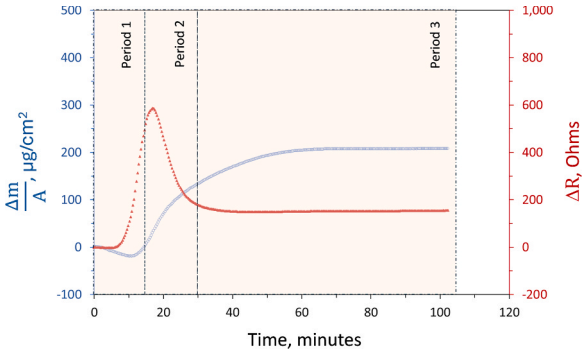

Fig. 6. Calculated change in mass per unit area (open blue circles) and measured change in motional resistance (solid red triangles) versus time for Scenario (b) with $FeCO_3$ formation due to corrosion of iron coated QCR in 1 wt % aqueous NaCl solution at 80 °C and pH 6.6. Periods 1, 2 and 3 are described in the text.

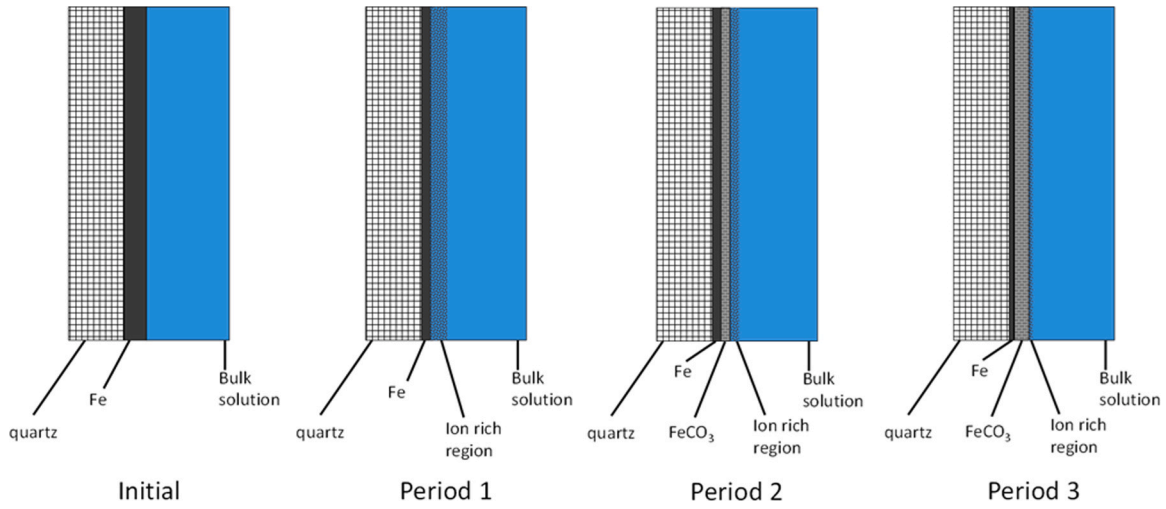

Fig. 7. Proposed schematic shows the substrate corrosion, evolution of near surface solution and corrosion product formation at different periods during the experiment for Scenario (b) with periods 1, 2 and 3 are described in the text.

because, in addition to diffusion of Fe^{2+} ions to the bulk solution, as discussed in Scenario (a), the formation of an $FeCO_3$ layer also consumes the Fe^{2+} ions, which depletes the ion rich layer and consequently leads to the decrease in the motional resistance. A delay in ΔR decrease is also noted, possibly due to the time required for sufficient amount of ions to be consumed by $FeCO_3$ formation.

Period 3: The decrease in resonance frequency (increase in added mass) indicates that the corrosion product layer continues to grow for some time until system has reached steady state, *i.e.* mass loss due to corrosion of the iron substrate balances out with the mass gain due to $FeCO_3$ precipitation. Corrosion rate slows down due to formation of $FeCO_3$ layer, and the precipitation rate slows down because Fe^{2+} ion concentration approaches saturation.

3.3. *Scenario (c):* $FeCO_3$ *formation on an iron coated crystal driven by bulk supersaturation*

Fig. 8 shows the measured frequency change (Δf) and calculated Gamma change (ΔΓ) where the $FeCO_3$ corrosion product formation on the iron substrate occurred due to high bulk supersaturation. Inferences drawn from Fig. 8 provide valuable insights into experimental observations. Notably, the absence of iron substrate corrosion from the QCR is observed with no change in Δf or $\frac{\Delta m}{A}$ during the first few minutes of the test, a departure from the findings in Scenario (b). This absence can be attributed to the specific experimental conditions employed. Under the highly supersaturated conditions utilized in this experiment, the process of $FeCO_3$ formation starts from the very onset of the experiment with no significant Fe^{2+} ion buildup required. If any initial mass loss due to corrosion occurred, it was offset by a simultaneous mass gain from $FeCO_3$ deposition, resulting in a flat mass-change curve as seen in the early stages of the experiment. Once precipitation dominated, the net mass gain becomes evident. The growing $FeCO_3$ layer subsequently lowered the corrosion rate [1–6], thereby further justifying the observed diminishing mass loss process and the subsequent net mass gain over time.

A noteworthy observation is the increase in motional resistance, as depicted in Fig. 9, which resembles the patterns observed previously (Scenario (a) and Scenario (b)); occurring prior to the observed mass change. This rise in motional resistance is associated with the formation of the Fe^{2+} ion rich layer resulting from the corrosion of the iron-coated substrate. Even when the substrate is cathodically polarized and bulk solution is supersaturated, corrosion current is not zero and hence limited Fe^{2+} release likely occurs. Though undetectable via Δf, the motional resistance signal captured this viscoelastic change and underscores the sensitivity of QCM to interfacial phenomena. The time axis is split into three zones in Fig. 9 which are explained with respect to the

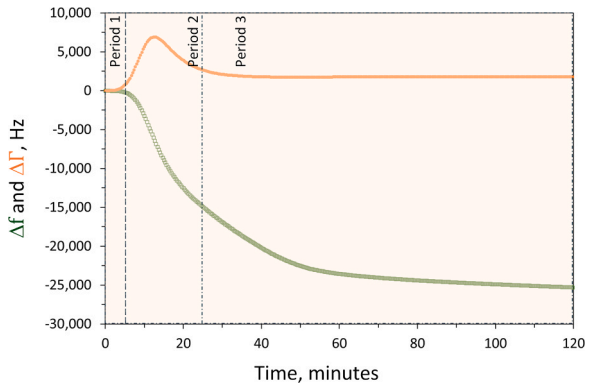

Fig. 8. Measured change in resonant frequency (open green squares) and calculated change in gamma (solid orange circles) versus time for Scenario (c) with $FeCO_3$ formation due to supersaturation on iron coated QCR in 1 wt% aqueous NaCl solution at 80 °C and pH 6.6 and under applied cathodic potential. Periods 1, 2 and 3 are described in the text.

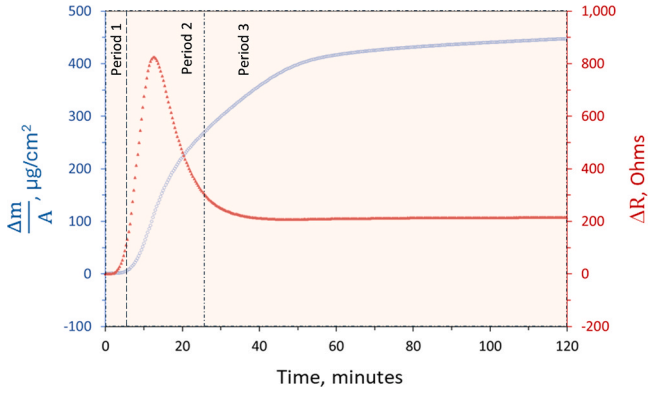

Fig. 9. Calculated change in mass per unit area (open blue circles) and measured change in motional resistance (solid red triangles) versus time for Scenario (c) with $FeCO_3$ formation due to supersaturation on iron coated QCR in 1 wt% aqueous NaCl solution at 80°C and pH 6.6 and under applied cathodic potential. Periods 1, 2 and 3 are described in the text.

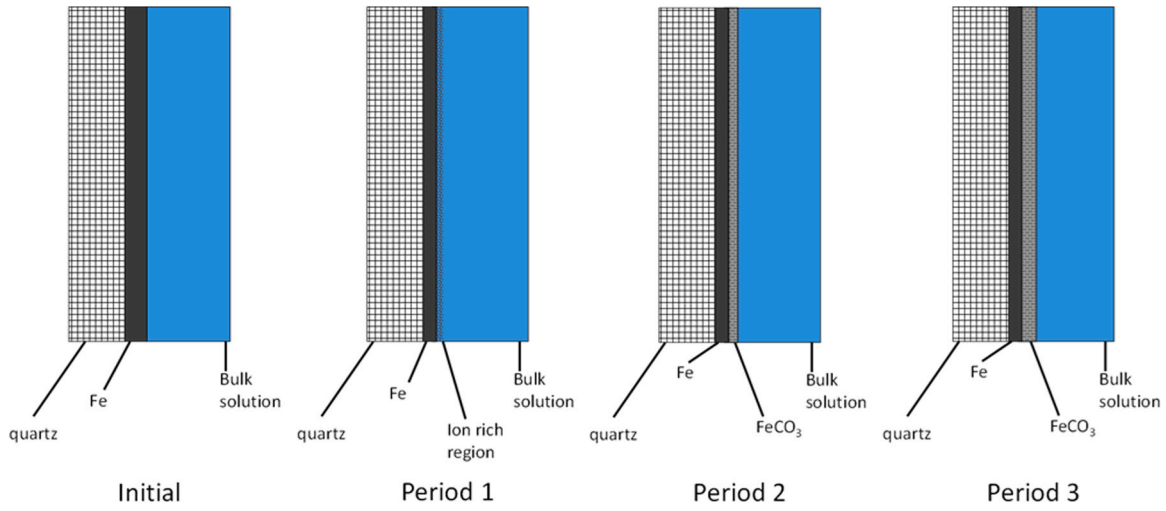

Fig. 10. Proposed schematic shows the diminished substrate corrosion as compared to Scenario (b), evolution of near surface solution and corrosion product formation and growth at different periods during the experiment. Periods 1, 2 and 3 are described in the text.

proposed schematic of events in Fig. 10 below:

Period 1: Characterized by a flat mass change curve due to the near-equilibrium between substrate corrosion and $FeCO_3$ precipitation, while motional resistance increased related to the build-up of an ion-rich interfacial layer.

Period 2: Net mass gain dominates, corresponding to $FeCO_3$ layer growth. Interestingly, a pronounced ΔR peak appears in this zone, hypothesized as a delayed response to the ion-rich layer formation in Period 1 rather than a direct consequence of precipitation of $FeCO_3$.

Period 3: Corrosion product layer growth continues until reaching a dynamic equilibrium. Motional resistance gradually decreases and stabilizes, consistent with the formation of a rigid, well-adhered $FeCO_3$. Decrease in motional resistance can be attributed to two factors: consumption of Fe^{2+} ions for the formation of $FeCO_3$ and further reduction in substrate corrosion rate (and hence lower Fe^{2+} near the substrate surface) due to the formation of protective $FeCO_3$ layer.

However, the direct correlation between the corrosion of the iron substrate and the observed increase in motional resistance which was implied needs verification. Further investigation is crucial for enhancing understanding of the complex interplay between corrosion processes and $FeCO_3$ formation in iron-coated QCR systems. Additional experiments defined by Scenario (d) and Scenario (e) aim to conclusively resolve the matter by examining the $FeCO_3$ formation on a gold coated QCR.

3.4. *Scenario (d):* $FeCO_3$ *formation on a gold coated crystal driven by bulk supersaturation*

To isolate $FeCO_3$ precipitation mechanisms, gold-coated quartz crystals were used as an inert substrate in a supersaturated solution (pH 6.6, 80 °C) prepared by $FeCl_2.4H_2O$ addition. As there was no other source of Fe^{2+} ions, any $FeCO_3$ layer growth could be attributed solely to precipitation from solution. Surface analysis of the formed layer on different substrates is presented in supplementary information (S2).

Fig. 11 shows the measured frequency change (Δf) and calculated Gamma change (ΔΓ) over the course of the experiment. Clearly, the governing condition ($|\Delta f| >> |\Delta\Gamma|$) is fulfilled, and hence measured frequency change can be converted into mass change per unit area using Sauerbrey's equation. As seen in Fig. 11, a steady decrease in resonance frequency (Δf) is the result of a steady mass gain, corresponding to $FeCO_3$ layer formation. There is no sudden increase of motional resistance for the gold substrate (Fig. 12) as compared to the previous three scenarios with an iron coated QCR. The fact that there was no increase of the motional resistance for the gold substrate serves as a supporting argument for the initial hypothesis of a direct relationship between the buildup of Fe^{2+} ions in the surface layer due to corrosion and the increase of motional resistance. This behavior also contrasts prior reports [11,12] that suggest ΔR spikes arise from $FeCl_2$ injection, which implies that such transient effects are not due to $FeCl_2$ itself, but due to a surface-specific reaction like corrosion, which is absent on the inert gold

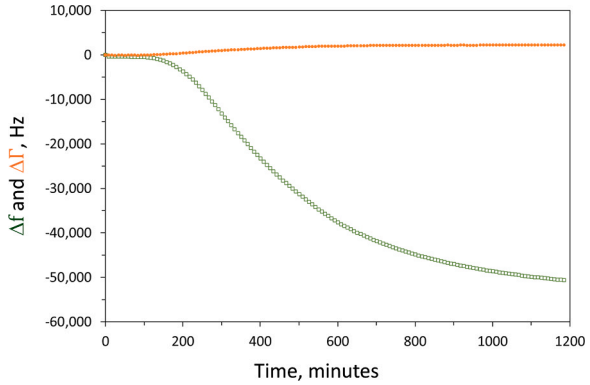

Fig. 11. Measured change in resonant frequency (open green squares) and calculated change in gamma (solid orange circles) versus time for Scenario (d) with $FeCO_3$ formation due supersaturation on gold coated QCR in 1 wt% aqueous NaCl solution at 80 °C and pH 6.6 under applied potential.

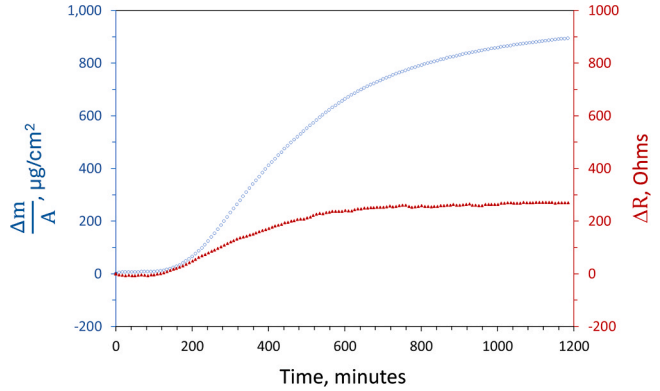

Fig. 12. Calculated change in mass per unit area (open blue circles) and measured change in motional resistance (solid red triangles) versus time for Scenario (d) with $FeCO_3$ formation due supersaturation on gold coated QCR in 1 wt% aqueous NaCl solution at 80 °C and pH 6.6 under applied potential.

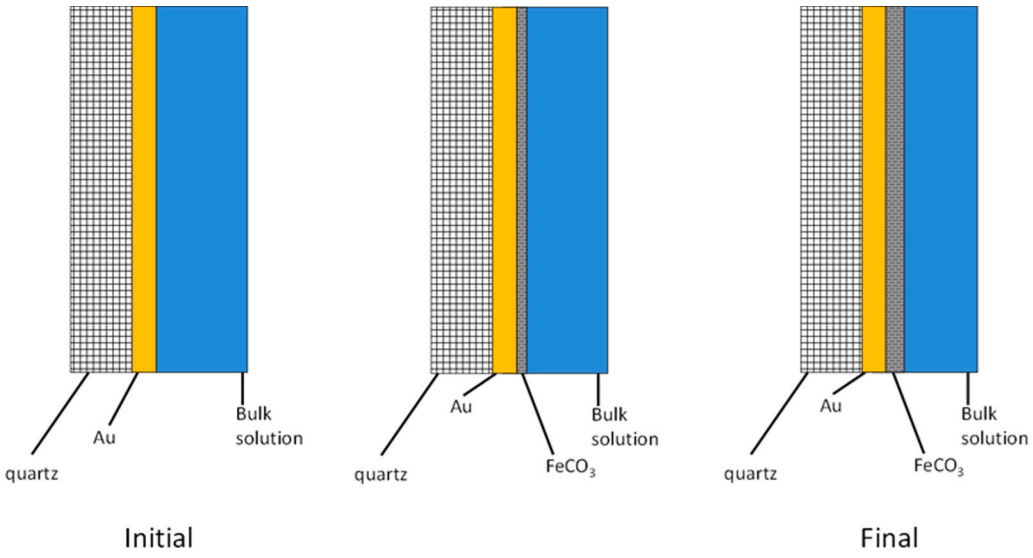

Fig. 13. Proposed schematic shows $FeCO_3$ formation and growth during the experiment for Scenario (d).

surface. The proposed schematic of events is illustrated in Fig. 13.

Furthermore, paying attention to the time axis for Scenario (c) and Scenario (d), the initiation and kinetics of the formation of $FeCO_3$ is different for these two different types of substrates: slower for the gold substrate but ending up with a higher total mass gain. Although the answer to why kinetics is different in the two scenarios of precipitation on gold and iron is not known yet, it can be speculated that the level of supersaturation in the near surface layer of solution is higher due to the contribution of corrosion (increase in Fe^{2+} ions) making the initial precipitation layer rate faster versus an inert, "defect free" gold surface. Overall, the precipitation of $FeCO_3$ on iron happens on a corroding substrate what possibly makes it more difficult in the "long run" and hence the overall mass of precipitated $FeCO_3$ is lower. While plausible, these explanations remain speculative and warrant further investigation.

3.5. *Scenario (e):* $FeCO_3$ *formation on a gold coated crystal driven by bulk supersaturation in highly concentrated brine (10 wt%* NaCl*)*

In this scenario, motional resistance in QCM data reflects the changes happening near the surface of the crystal. Not only does the layer formation influence the QCM response but also changes in the near-surface solution properties, such as density and viscosity, which can lead to changes in the frequency and motional resistance response [28,55,56].

In non-ideal solutions, viscosity and density differ from those of more dilute solutions due to the changes in ion interactions. Therefore, these parameters must be adjusted for non-ideal brines using either empirical relations or experimental measurements. Before proceeding with the main experiments in this study, the relationship between density and viscosity of the solution versus NaCl concentration was measured using QCM response and compared to existing models.

Experimental measurements were performed in a 2-liter glass cell at 30 °C. The solution was deoxygenated with CO_2 prior to the experiment and sparged throughout the test to ensure that no oxygen was present in the system. pH of the solution was autogenous and remained constant throughout the experiment. Gold-coated QCR response, including frequency change when moving the crystal from air to the solution, and motional resistance, was recorded at different NaCl concentrations and presented in Fig. 14. It can be noted that frequency change as well as the motional resistance are higher in a more concentrated solution. Change in resonance frequency with change of the medium can be related by Kanazawa's equation [55]:

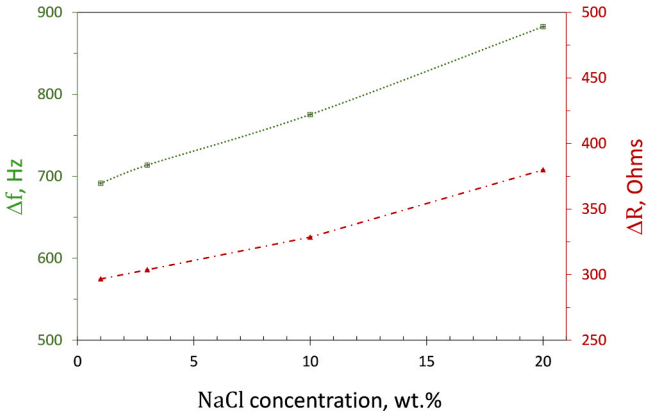

Fig. 14. Measured change in resonance frequency (open green squares) and motional resistance (solid red triangles) versus NaCl concentration and on gold-coated QCR at 30 °C.

$$\Delta f = -f_2^3 \left(\frac{\rho_{solution} \mu_{solution}}{\pi \rho_q \eta_q} \right)^{\frac{1}{2}} \tag{7}$$

where $\rho_{solution}$ and ρ_q are solution density and quartz density, respectively (g/cm^3), $\mu_{solution}$ is the solution viscosity (g/cm·s) and η_q is the quartz shear modulus (g/cm·s^2). From that, products of solution density and viscosity can be found and compared to existing models.

Various models have been proposed to account for the hydrodynamic properties of concentrated NaCl solutions. For a deeper understanding of the effect of NaCl on solution transport parameters, the reader is referred to the publication that reviews different models available in the literature [47]. For this study, two models were selected for calculating solution density and viscosity.

Solution density was calculated using Batzle and Wang equation [57]:

$$\rho_{solution} = \rho_{water} + S(0.668 + 0.44S + 10^{-6}(300P - 2400PS + T_C(80 + 3T_C - 3300S - 13P + 47PS)) \tag{8}$$

where ρ_{water} is water density (g/cm^3), P is total pressure (MPa), T_C is solution temperature (°C), and S is mass fraction of salt.

Solution viscosity changes not only with salt concentration but also under CO_2-saturated conditions. To account for that, a combination of Mao and Duan [58] and Islam and Carlson [59] models were used:

$$\mu_{solution} = \mu_{brine}(1 + 4.65x_{CO_2}^{0.0144T_K - 3.3964}) \quad (9)$$

where $\mu_{solution}$ is solution viscosity in the presence of water, NaCl, and CO_2, x_{CO_2} is the mole fraction of dissolved CO_2, T_K is temperature in Kelvin, and μ_{brine} is the density of the solution in the presence of NaCl only.

In addition to the frequency change response obtained during the experiment, the motional resistance response was also recorded. Motional resistance response is sensitive to solution properties such as solution density and viscosity according to the following relation [60, 61]:

$$\Delta R = \left(\frac{n_s \omega_s L_u}{\pi}\right)\left(\frac{2\omega_s \rho_{solution}\mu_{solution}}{\rho_q \eta_q}\right)^{\frac{1}{2}} \quad (10)$$

where n_s is the number of sides in contact with the solution, ω_s is angular frequency, L_u is the undisturbed resonator inductance.

Fig. 15 compares products of solution density and viscosity measurements obtained from QCM response to the ones calculated using the above-mentioned model at various NaCl concentrations. Experimental measurements from QCM showed a good agreement with the above-mentioned model, with slight discrepancies that can be attributed to the limitations of the models as well as experimental uncertainties. Experimental QCM measurements have shown that brine properties change under varying salt conditions. This finding will be used in this study to explain phenomena happening near the quartz crystal in precipitation conditions at 10 wt% aqueous NaCl solution, 80 °C and pH 6.4.

Fig. 16 presents the relation between the change in motional resistance and product of solution density and viscosity calculated using the Butterworth-Van Dyke equivalent circuit model for different NaCl concentrations. There is a linear relationship between ΔR and $(\rho_{solution}\mu_{solution})^{1/2}$ suggesting the validity of the experimental data acquired using QCM.

Fig. 17 and Fig. 18 present Δf compared to ΔΓ; and mass change and ΔR, respectively. The results obtained at a non-ideal 10 wt% NaCl solution were consistent with observations in Scenario (d): similar trends in mass change increase as $FeCO_3$ precipitated on a gold substrate, as well as a gradual rise in motional resistance without sudden peaks until it reached a steady-state value. This suggests that mass precipitation evolution near the surface at non-ideal conditions is comparable to that at 1 wt% NaCl. The proposed schematic of events is illustrated in Fig. 19.

Although previously reported findings suggested that the precipitation rate of $FeCO_3$ is independent of NaCl concentration [39], faster precipitation was observed in the 10 wt% NaCl solution, as indicated by steeper mass and motional resistance slopes. This difference appears to result from the slightly more cathodic polarization applied in the case of 10 wt% NaCl solution. During preliminary trials, the QCR showed minimal mass deposition at −0.72 $V_{Ag/AgCl}$ in 10 wt% NaCl, therefore, it was necessary to lower the applied polarization potential to −0.75 $V_{Ag/AgCl}$ to get comparable mass deposition. The more cathodic potential

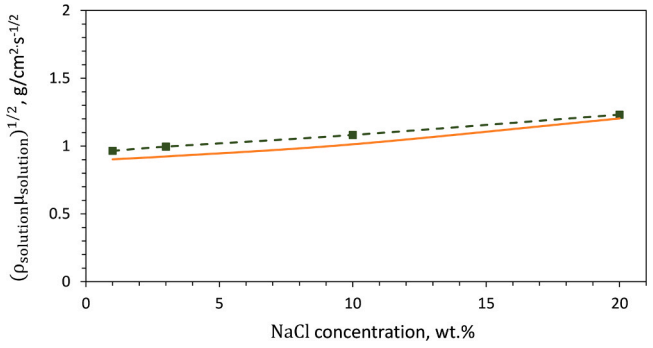

Fig. 15. Product of square root of density and viscosity of aqueous NaCl solution calculated using Kanazawa's equation from experiment (solid green squares) and calculated using a combination of Mao and Duan [58] and Islam and Carlson [59] models (orange curve) versus NaCl concentration and on gold-coated QCR at 30 °C.

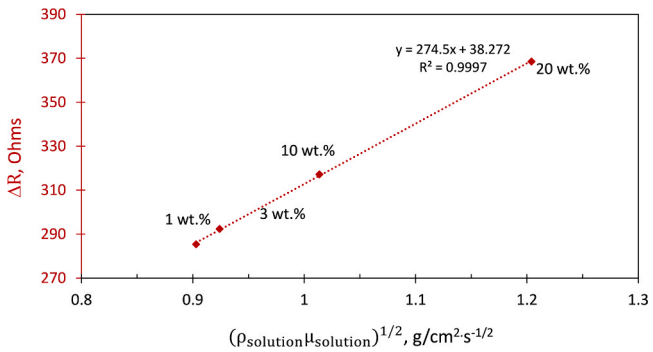

Fig. 16. Motional resistance change response versus product of square root of density and viscosity of aqueous NaCl solution calculated using a combination of Mao and Duan [55] and Islam and Carlson [56] models at different NaCl concentrations on gold-coated QCR at 30 °C.

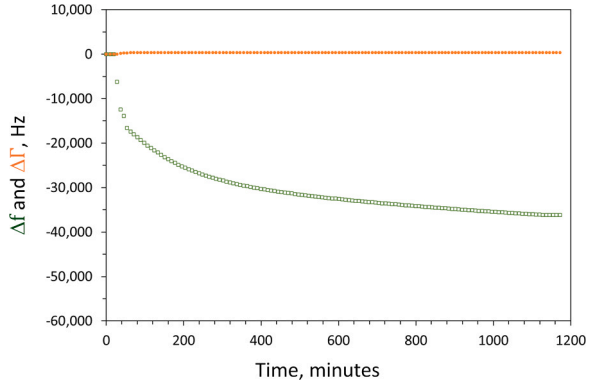

Fig. 17. Measured change in resonance frequency (open green squares) and calculated change in gamma (solid orange circles) versus time for Scenario (e) with $FeCO_3$ formation due to supersaturation on gold coated QCR in 10 wt% aqueous NaCl solution at 80 °C and pH 6.4 under applied potential.

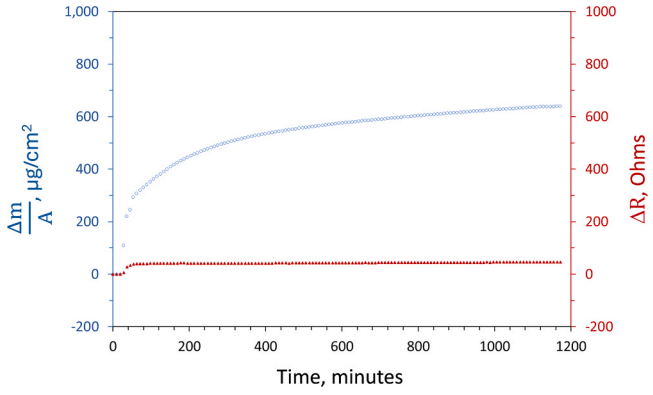

Fig. 18. Calculated change in mass per unit area (open blue circles) and measured change in motional resistance (solid red triangles versus time for Scenario (e) with $FeCO_3$ formation due to supersaturation on gold coated QCR in 10 wt% aqueous NaCl solution at 80°C and pH 6.4 under applied potential.

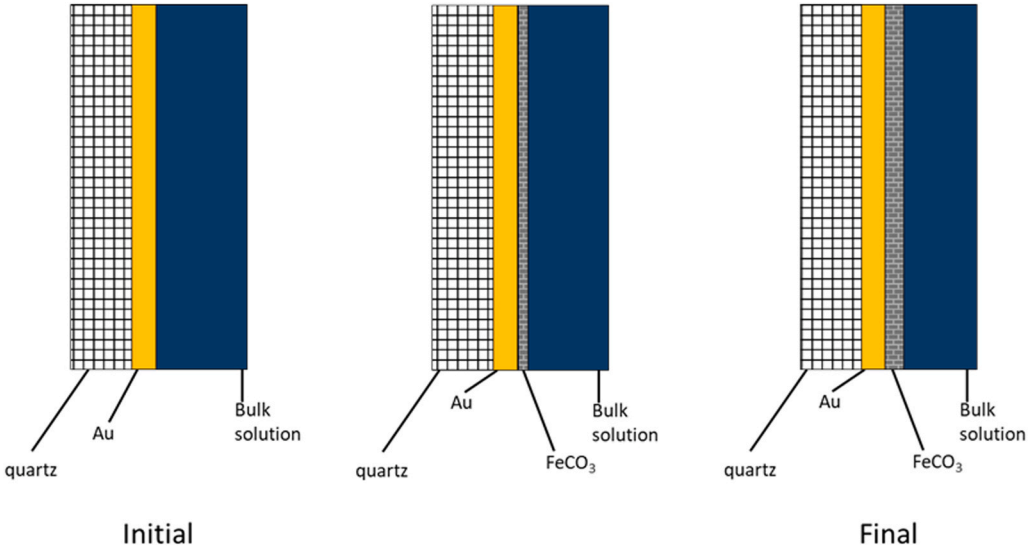

Fig. 19. Proposed schematic shows $FeCO_3$ formation and growth during the experiment for Scenario (e).

enhanced hydrogen evolution, increasing local pH and surface supersaturation, thereby facilitating $FeCO_3$ formation. Additionally, the non-ideal behavior of the 10 wt% NaCl solution complicates replication of near-surface conditions observed in dilute solutions such as 1 wt% NaCl solution. Therefore, the observed increase in precipitation rate in the 10 wt% NaCl solution is attributed primarily to the change in polarization voltage rather than solution concentration.

Another discrepancy can be seen in the measured motional resistance values at the end of experiment. This difference is hypothesized to arise from variations in solution properties rather than differences in the $FeCO_3$ layer itself. Motional resistance depends not only on the deposited mass but also on the interaction between the surface and the solution near it. For example, the higher density and viscosity of 10 wt% NaCl resulted in higher initial motional resistance values (*ca.* 287 Ω) compared to 1 wt% NaCl (221–235 Ω) under otherwise similar conditions as it can be seen in Fig. 14. Because the density and viscosity of the 10 wt% NaCl solution are closer to those of the $FeCO_3$ layer, the difference in mechanical response between the layer and the solution is smaller, producing a smaller overall change in motional resistance. Conversely, in 1 wt% NaCl solution, the larger contrast amplifies the effect of the layer on resistance, leading to a more pronounced increase. While this explanation is consistent with the observed trends, it remains speculative and requires further investigation, particularly for concentrated, non-ideal brines.

4. Conclusions

This study demonstrates that $FeCO_3$ formation dynamics and corrosion behavior can be effectively studied using QCM. Across all scenarios, whether involving inert or active substrates, with or without an external source of Fe^{2+}, analyzing motional resistance or half width at half height of the quartz resonator conductance (Gamma) in conjunction with mass change has helped in developing a deeper understanding of the physical processes happening on the metal surface.

- **On iron substrates (Scenarios a, b and c):**
  - In the absence of precipitation (Scenario (a)), ΔR increased without associated mass gain, indicating Fe^{2+} ion buildup in the surface layer of solution due to corrosion and therefore, the interfacial electrolyte properties must be taken into account.
  - The scenarios where $FeCO_3$ layer forms, (with and without external Fe^{2+} addition – Scenarios (c) and (b) respectively) show ΔR peaks associated with an ion-rich interfacial layer produced by active iron dissolution. This layer, even if not detectable via. frequency change response of QCM, is effectively captured by associated changes in motional resistance.
  - Frequency or mass change response is instantaneous, however there is a considerable lag in motional resistance response which is related to the time required for buildup of ions in the solution near the substrate surface.
  - Even at the bulk saturation of 600 in the case of iron coated crystal and under applied cathodic potential, corrosion of the base material still happens, which was not conclusively evident from only the mass change curve. Analysis of the motional resistance response provides experimental proof of corrosion of the substrate even in supersaturated conditions.

- **On gold substrates (Scenarios d and e):**
  - The lack of ΔR transients confirms that changes in motional resistance are not caused by $FeCl_2.4H_2O$ addition or bulk solution effects.
  - Initiation and kinetics of $FeCO_3$ formation are different for different types of substrates, here discussed for iron and gold.

Collectively, these findings show that motional resistance response from QCM is a powerful, yet underutilized, tool that can provide valuable information of early interfacial dynamics in corrosion–precipitation systems. While the frequency-change response primarily tracks mass, ΔR reveals subtleties of ion accumulation, transport, and changes in near surface solution properties. By comparing inert and active substrates under different chemical driving forces, this study clarifies the mechanistic origins of transient responses captured using QCM and expands its value as a diagnostic tool in corrosion science.

CRediT authorship contribution statement

Kushal Singla: Writing – review & editing, Writing – original draft, Visualization, Validation, Methodology, Investigation, Formal analysis, Data curation, Conceptualization. **Kamila Turganova:** Writing – review & editing, Writing – original draft, Visualization, Validation, Methodology, Investigation, Formal analysis, Data curation. **Bruce Brown:** Writing – review & editing, Supervision, Resources, Project administration, Funding acquisition. **Hubert Perrot:** Writing – review & editing, Validation, Supervision, Formal analysis. **Srdjan Nešić:** Writing – review & editing, Supervision, Project administration, Funding

acquisition, Formal analysis, Conceptualization. **Sahithi Ayyagari:** Writing – review & editing, Writing – original draft, Visualization, Validation, Methodology, Investigation, Formal analysis, Data curation, Conceptualization.

Declaration of Competing Interest

The authors declare that they have no known competing financial interests or personal relationships that could have appeared to influence the work reported in this paper.

Acknowledgments

The authors would like to thank the following companies for their financial support: Ansys, Baker Hughes, ChampionX LLC, Chevron Energy Technology, Coastal Chemical Co., ConocoPhillips, ExxonMobil, M-I SWACO (Schlumberger), Occidental Oil Company, Pertamina, Saudi Aramco, Shell Global Solutions and TotalEnergies.

Appendix A. Supporting information

Supplementary data associated with this article can be found in the online version at doi:10.1016/j.corsci.2026.113910.

Data availability

Data will be made available on request.

References

[1] M. Nordsveen, S. Nešić, R. Nyborg, A. Stangeland, A mechanistic model for carbon dioxide corrosion of mild steel in the presence of protective iron carbonate films—part 1: theory and verification, Corrosion 59 (2003) 443–456, https://doi.org/10.5006/1.3277576.
[2] R. Jacklin, J. Owen, A. Sykes, D. Burkle, R.C. Woollam, R. Barker, An electrochemical study of iron carbonate layers formed on carbon steel during corrosion in elevated pressure CO2 environments, Corros. Sci. 235 (2024) 112202, https://doi.org/10.1016/j.corsci.2024.112202.
[3] A. Dugstad, Mechanism of protective film formation during CO2 corrosion of carbon steel, in: CORROSION, Paper No. 98031, NACE, Houston, TX, 1998.
[4] R. Barker, D. Burkle, T. Charpentier, H. Thompson, A. Neville, A review of iron carbonate (FeCO3) formation in the oil and gas industry, Corros. Sci. 142 (2018) 312–341, https://doi.org/10.1016/j.corsci.2018.07.021.
[5] J. Greenberg, M. Tomson, Precipitation and dissolution kinetics and equilibria of aqueous ferrous carbonate vs temperature, Appl. Geochem. 7 (1992) 185–190, https://doi.org/10.1016/0883-2927(92)90036-3.
[6] M. Honarvar Nazari, S.R. Allahkaram, M.B. Kermani, The effects of temperature and pH on the characteristics of corrosion product in CO2 corrosion of grade X70 steel, Mater. Des. 31 (2010) 3559–3563, https://doi.org/10.1016/j.matdes.2010.01.038.
[7] M.H. Sk, A.M. Abdullah, M. Ko, B. Ingham, N. Laycock, R. Arul, DavidE. Williams, Local supersaturation and the growth of protective scales during CO2 corrosion of steel: effect of pH and solution flow, Corros. Sci. 126 (2017) 26–36, https://doi.org/10.1016/j.corsci.2017.05.026.
[8] D. Burkle, R. De Motte, W. Taleb, A. Kleppe, T. Comyn, S.M. Vargas, A. Neville, R. Barker, situ SR-XRD study of FeCO3 precipitation kinetics onto carbon steel in CO2-containing environments: The influence of brine pH, Electrochim. Acta 255 (2017) 127–144, https://doi.org/10.1016/j.electacta.2017.09.138.
[9] R. De Motte, E. Basilico, R. Mingant, J. Kittel, F. Ropital, P. Combrade, S. Necib, V. Deydier, D. Crusset, S. Marcelin, A study by electrochemical impedance spectroscopy and surface analysis of corrosion product layers formed during CO2 corrosion of low alloy steel, Corros. Sci. 172 (2020) 108666, https://doi.org/10.1016/j.corsci.2020.108666.
[10] S. Ayyagari, B. Brown, S. Nesic, Effect of acetic acid on corrosion product layer formation in aqueous CO2 environments, in: CORROSION, Paper No. 19306, AMPP, Houston, TX, 2023.
[11] Z. Ma, Y. Yang, B. Brown, S. Nesic, M. Singer, Investigation of precipitation kinetics of FeCO3 by EQCM, Corros. Sci. 141 (2018) 195–202, https://doi.org/10.1016/j.corsci.2018.06.017.
[12] Z. Ma, Precipitation Kinetics of FeCO3 and FeS on Steel Substrate(PhD Dissertation), Ohio University, 2021.
[13] R.A. De Motte, R. Barker, D. Burkle, S.M. Vargas, A. Neville, The early stages of FeCO3 scale formation kinetics in CO2 corrosion, Mater. Chem. Phys. 216 (2018) 102–111, https://doi.org/10.1016/j.matchemphys.2018.04.077.
[14] A. Matamoros-Veloza, R. Barker, S. Vargas, A. Neville, Mechanistic insights of dissolution and mechanical breakdown of FeCO3 corrosion films, ACS Appl. Mater. Interfaces 13 (2021) 5741–5751, https://doi.org/10.1021/acsami.0c18976.
[15] M. Di Bonaventura Fruno, Effect of Flow on the Formation of Iron Carbonate and Influence of Exposed Iron Carbide Layer(MS Thesis), Ohio University, 2017.
[16] V. Ruzic, M. Veidt, S. Nešić, Protective iron carbonate films—part 1: mechanical removal in single-phase aqueous flow, Corrosion 62 (2006) 419–432, https://doi.org/10.5006/1.3278279.
[17] V. Ruzic, M. Veidt, S. Nešić, Protective iron carbonate films—part 3: simultaneous chemo-mechanical removal in single-phase aqueous flow, Corrosion 63 (2007) 758–769, https://doi.org/10.5006/1.3278425.
[18] J. bin Han, Y. Yang, B. Brown, S. Nesic, Electrochemical investigation of localized CO2 corrosion on mild steel, in: CORROSION, Paper No. 07323, NACE, Houston, TX, 2007.
[19] W. Li, B. Brown, D. Young, S. Nesic, Investigation of pseudo-passivation of mild steel in CO2 corrosion, in: CORROSION, Paper No. 2149, NACE, Houston, TX, 2013.
[20] H. Mansoori, D. Young, B. Brown, S. Nešić, M. Singer, CO2 corrosion of mild steel exposed to CaCO3-saturated aqueous solutions, Corrosion 75 (2019) 1281–1284, https://doi.org/10.5006/3310.
[21] E. Van Hunnik, E.L.J.A. Hendriksen, B.F.M. Pots, The formation of protective FeCO3 corrosion product layers in CO2 corrosion, in: CORROSION, Paper No. 96006, NACE, Houston, TX, 1996.
[22] S. Ieamsupapong, B. Brown, M. Singer, S. Nesic, Effect of solution PH on corrosion product layer formation in a controlled water chemistry system, in: CORROSION, Paper No. 9160, NACE, Houston, TX, 2017.
[23] T. Tanupabrungsun, Thermodynamics and Kinetics of Carbon Dioxide Corrosion of Mild Steel at Elevated Temperatures(PhD Dissertation), Ohio University, 2012. ⟨http://rave.ohiolink.edu/etdc/view?acc_num=ohiou1355328679⟩.
[24] B. Ingham, M. Ko, N. Laycock, N.M. Kirby, D.E. Williams, First stages of siderite crystallisation during CO2 corrosion of steel evaluated using in situ synchrotron small- and wide-angle X-ray scattering, Faraday Discuss. 180 (2015) 171–190, https://doi.org/10.1039/C4FD00218K.
[25] B. Ingham, M. Ko, N. Laycock, J. Burnell, P. Kappen, J.A. Kimpton, D.E. Williams, situ synchrotron X-ray diffraction study of scale formation during CO2 corrosion of carbon steel in sodium and magnesium chloride solutions, Corros. Sci. 56 (2012) 96–104, https://doi.org/10.1016/j.corsci.2011.11.017.
[26] D. Burkle, R. De Motte, W. Taleb, A. Kleppe, T. Comyn, S.M. Vargas, A. Neville, R. Barker, Development of an electrochemically integrated SR-GIXRD flow cell to study FeCO3 formation kinetics, Rev. Sci. Instrum. 87 (2016) 105125, https://doi.org/10.1063/1.4965971.
[27] J. Owen, D. Burkle, G.R. Joshi, E. Basilico, J. Kittel, F. Ropital, S. Marcelin, A. Kleppe, R.C. Woollam, R. Barker, situ SR-XRD analysis of corrosion product formation during 'pseudo-passivation' of carbon steel in CO2-containing aqueous environments, Corros. Sci. 225 (2023) 111598, https://doi.org/10.1016/j.corsci.2023.111598.
[28] M. Hepel, Electrode-solution interface studied with electrochemical quartz crystal nanobalance, in: A. Wieckowski (Ed.), Interfacial Electrochemistry Theory: Experiment, and Applications, 1st ed., Taylor and Francis Group, New York, 1999, pp. 599–630.
[29] G. Sauerbrey, Verwendung von Schwingquarzen zur Wägung dünner Schichten und zur Mikrowägung, Z. F. üR. Phys. 155 (1959) 206–222, https://doi.org/10.1007/BF01337937.
[30] A. Cuenca, J. Agrisuelas, J.J. García-Jareño, F. Vicente, Oscillatory changes of the heterogeneous reactive layer detected with the motional resistance during the galvanostatic deposition of copper in sulfuric solution, Langmuir 31 (2015) 12664–12673, https://doi.org/10.1021/acs.langmuir.5b03694.
[31] A. Cuenca, J. Agrisuelas, R. Catalán, J.J. García-Jareño, F. Vicente, Motional resistance evaluation of the quartz crystal microbalance to study the formation of a passive layer in the interfacial region of a copper|diluted sulfuric solution, Langmuir 31 (2015) 9655–9664, https://doi.org/10.1021/acs.langmuir.5b02233.
[32] S.K. Mohanty, Y. Ok, E.S. Kim, Y. Park, J.H. Ryu, J. Mun, J. Lee, K. Hyun, M. K. Srinivasa, H. Jeong, S.C. Reddy, H.D. Yoo, Motional resistance as highly selective descriptor to probe dynamic formation of surface films on zinc anode, Batter. Supercaps. 7 (2024) e202400338, https://doi.org/10.1002/batt.202400338.
[33] K. Singla, H. Perrot, O. Sel, B. Brown, S. Nesic, Use of quartz crystal microbalance in study of inhibitor adsorption, in: CORROSION, Paper No. 16653, AMPP, Houston, TX, 2021.
[34] K. Singla, H. Perrot, B. Brown, S. Nesic, Adsorption of model inhibitor compound characterized using quartz crystal microbalance with dissipation monitoring, in: CORROSION, Paper No. 19145, AMPP, Houston, TX, 2023.
[35] K. Singla, H. Perrot, B. Brown, S. Nešić, Quantification of the adsorption kinetics of a model corrosion inhibitor on gold using QCM-D, Corrosion 80 (2024) 1207–1215, https://doi.org/10.5006/4634.
[36] Y. Ding, Mechanistic Understanding of CO2 Corrosion Inhibition at Elevated Temperatures(PhD Dissertation), Ohio University, 2019. ⟨http://rave.ohiolink.edu/etdc/view?acc_num=ohiou1547122087551426⟩.
[37] A. Chandra, W. Durnie, J. Vera, R. Woolam, Relationship between inhibitor adsorption and surfactant properties: part II - critical parameters, in: CORROSION, Paper No. 13245, NACE, Houston, TX, 2019.
[38] C. Valero Vidal, A. Igual Muñoz9 - Influence of protein adsorption on corrosion of biomedical alloys, in: Y. Yan (Ed.), Bio-Tribocorrosion in Biomaterials and Medical Implants, Woodhead Publishing, 2013: pp. 187–219. https://doi.org/https://doi.org/10.1533/9780857098603.2.187.
[39] Z. Ma, X. Gao, B. Brown, S. Nesic, M. Singer, Improvement to water speciation and FeCO3 precipitation kinetics in CO2 environments: updates in NaCl concentrated solutions, Ind. Eng. Chem. Res. 60 (2021) 17026–17035, https://doi.org/10.1021/acs.iecr.1c02957.

[40] Z. Ma, B. Brown, S. Nesic, M. Singer, Investigation of FeS precipitation kinetics by EQCM, in: CORROSION, Paper No. 13425, NACE, 2019.
[41] W. Sun, S. Nešić, R.C. Woollam, The effect of temperature and ionic strength on iron carbonate (FeCO3) solubility limit, Corros. Sci. 51 (2009) 1273–1276, https://doi.org/10.1016/j.corsci.2009.03.009.
[42] D. Johannsmann, Introduction, in: D. Johannsmann (Ed.), The Quartz Crystal Microbalance in Soft Matter Research: Fundamentals and Modeling, Springer International Publishing, Cham, 2015, pp. 1–22, https://doi.org/10.1007/978-3-319-07836-6_1.
[43] D. Johannsmann, Modeling the resonator as a parallel plate, in: D. Johannsmann (Ed.), The Quartz Crystal Microbalance in Soft Matter Research: Fundamentals and Modeling, Springer International Publishing, Cham, 2015, pp. 49–123, https://doi.org/10.1007/978-3-319-07836-6_4.
[44] C. Gabrielli, A.A.O. Magalhaes, I.C.P. Margarit, H. Perrot, B. Tribollet, Study of chromate–zinc conversion process through microbalance/electroacoustic impedance coupling measurements, Electrochem. Commun. 6 (2004) 492–498, https://doi.org/10.1016/j.elecom.2004.02.017.
[45] D. Johannsmann, Essentials of viscoelasticity, in: D. Johannsmann (Ed.), The Quartz Crystal Microbalance in Soft Matter Research: Fundamentals and Modeling, Springer International Publishing, Cham, 2015, pp. 33–47, https://doi.org/10.1007/978-3-319-07836-6_3.
[46] D. Johannsmann, I. Reviakine, Quartz crystal microbalance with dissipation monitoring for studying soft matter at interfaces, Nat. Rev. Methods Prim. 4 (2024) 63, https://doi.org/10.1038/s43586-024-00340-4.
[47] F. Madani Sani, S. Nesic, A critical review of models for density, viscosity, and diffusivity in aqueous sodium chloride solutions, Electrochim. Acta 477 (2024) 143766, https://doi.org/10.1016/j.electacta.2024.143766.
[48] Operations and Service Manual-QCM200 Quartz Crystal Microbalance, Sunnyvale, California, 2004.
[49] W. Li, Investigation of Pseudo-Passive Layer Formation in CO2 Corrosion(MS Thesis), Ohio University, 2011.
[50] Y. Yang, Removal Mechanisms of Protective Iron Carbonate Layer in Flowing Solutions(PhD Dissertation), Ohio University, 2012.
[51] X. Gao, Localized Corrosion Initiation of Steel in CO2 Environments. PhD Dissertation, Ohio University, 2020.
[52] S. Nešić, A. Kahyarian, Y.S. Choi, Implementation of a comprehensive mechanistic prediction model of mild steel corrosion in multiphase oil and gas pipelines, Corrosion 75 (2018) 274–291, https://doi.org/10.5006/3093.
[53] Institute for Corrosion and Multiphase Technology, Multicorp2020. ⟨https://www.icmt.ohio.edu/software/multicorp/multicorp%206/index.asp⟩ (accessed January 21, 2026).
[54] A. Kahyarian, Mechanism and Prediction of Mild Steel Corrosion in Aqueous Solutions Containing Carboxylic Acids, Carbon Dioxide, and Hydrogen Sulfide(PhD Dissertation), Ohio University, 2018. ⟨http://rave.ohiolink.edu/etdc/view?acc_num=ohiou1541154736282768⟩.
[55] K.Keiji Kanazawa, J.G. Gordon, The oscillation frequency of a quartz resonator in contact with liquid, Anal. Chim. Acta 175 (1985) 99–105, https://doi.org/10.1016/S0003-2670(00)82721-X.
[56] M. Urbakh, L. Daikhin, Surface morphology and the quartz crystal microbalance response in liquids, Colloids Surf. A Physicochem. Eng. Asp. 134 (1998) 75–84, https://doi.org/10.1016/S0927-7757(97)00334-8.
[57] M. Batzle, Z. Wang, Seismic properties of pore fluids, Geophysics 57 (1992) 1396–1408, https://doi.org/10.1190/1.1443207.
[58] S. Mao, Z. Duan, The viscosity of aqueous alkali-chloride solutions up to 623 K, 1,000 bar, and high ionic strength, Int. J. Thermophys. 30 (2009) 1510–1523, https://doi.org/10.1007/s10765-009-0646-7.
[59] A.W. Islam, E.S. Carlson, Viscosity models and effects of dissolved CO2, Energy & Fuels 26 (2012) 5330–5336, https://doi.org/10.1021/ef3006228.
[60] S.J. Martin, V.Edwards Granstaff, G.C. Frye, Characterization of a quartz crystal microbalance with simultaneous mass and liquid loading, Anal. Chem. 63 (1991) 2272–2281, https://doi.org/10.1021/ac00020a015.
[61] Hiroshi Muramatsu, Eiichi Tamiya, Isao Karube, Computation of equivalent circuit parameters of quartz crystals in contact with liquids and study of liquid properties, Anal. Chem. 60 (1988) 2142–2146, https://doi.org/10.1021/ac00170a032.